

27 Abstract

28
29 Volcanic calderas are surface depressions formed by roof collapse following evacuation of magma from
30 an underlying reservoir. The mechanisms of caldera formation are debated and predict differences in the
31 evolution of the caldera floor and distinct styles of magma recharge. Here we use a dense, active source,
32 seismic tomography study to reveal the sub-surface physical properties of the Santorini caldera in order
33 to understand caldera formation. We find a ~3-km-wide, cylindrical low-velocity anomaly in the upper 3
34 km beneath the north-central portion of the caldera, that lies directly above the pressure source of the
35 2011-2012 inflation. We interpret this anomaly as a low-density volume caused by excess porosities of
36 between 4% and 28%, with pore spaces filled with hot seawater. Vents that were formed during the first
37 three phases of the 3.6 ka Late Bronze Age (LBA) eruption are located close to the edge of the imaged
38 structure. The correlation between older volcanic vents and the low-velocity anomaly suggests that this
39 feature may be long-lived. We infer that collapse of a limited area of the caldera floor resulted in a high-
40 porosity, low-density cylindrical volume, which formed by either chaotic collapse along reverse faults,
41 wholesale subsidence and infilling with tuffs and ignimbrites, phreatomagmatic fracturing, or a
42 combination of these processes. Phase 4 eruptive vents are located along the margins of the topographic
43 caldera and the velocity structure indicates that coherent down-drop of the wider topographic caldera
44 followed the more limited collapse in the northern caldera. This progressive collapse sequence is
45 consistent with models for multi-stage formation of nested calderas along conjugate reverse and normal
46 faults. The upper crustal density differences inferred from the seismic velocity model predict differences
47 in subsurface gravitational loading that correlate with the location of 2011-2012 edifice inflation. This
48 result supports the hypothesis that sub-surface density anomalies may influence present-day magma
49 recharge events. We postulate that past collapses and the resulting topographical and density variations

50 at Santorini influence magma focusing between eruptive cycles, a feedback process that may be important
51 in other volcanoes.

52 1. Introduction

53 The mechanisms involved in the formation of volcanic calderas continue to be a matter of some debate,
54 in part due to their structural complexity as revealed by geological field studies. Proposed formational
55 models include multi-event piecemeal collapse (Williams, 1941), piston subsidence of a central plug
56 followed by erosion at the margins (Lipman, 1997; Walker, 1984), nested caldera formation along sets of
57 inward- and outward-dipping ring faults (Roche et al., 2000; Scandone and Acocella, 2007), and funnel-
58 shaped collapse into a cored-out volcanic vent (Aramaki, 1984; Escher, 1929; Yokoyama, 1981). Other clues
59 to caldera formation are provided by sandbox experiments and numerical model predictions of subsurface
60 stress and suggest that, as deformation and evacuation progress, the style of roof collapse evolves from
61 initial reverse faulting to later development of an outer ring of conjugate normal faults (Acocella, 2006;
62 Holohan et al., 2015).

63 Shallow low-velocity anomalies and caldera faults have previously been seismically imaged beneath
64 volcanoes and, in a few cases, seismicity has been detected along ring faults. At some large caldera systems,
65 such as Yellowstone (Farrell et al., 2015) and Campi Flegrei (Vanorio, 2005), these localized low-velocity
66 regions in the uppermost crust (<5 km) are explained as hydrothermal reservoirs. Elsewhere, for example
67 at Krakatoa (Deplus et al., 1995), Deception Island (Zandomenighi et al., 2009) and Newberry (Beachly et
68 al., 2012; Heath et al., 2015) volcanoes, the caldera is filled with low-velocity material interpreted to
69 correspond to sediments and brecciated caldera-fill. These low-velocity zones narrow downward and
70 connect to magmatic systems in the upper crust below ~2 km depth. At other volcanoes, displacement on
71 caldera ring faults has been inferred from seismicity recorded during dike and eruption episodes. At

72 Bárðarbunga earthquakes beneath the caldera delineate a tall (8-km high), slightly-tilted plug overlying the
73 inferred magma system (Gudmundsson et al., 2016). While at Axial Seamount conjugate inward- and
74 outward-facing faults were activated during inflation and deflation episodes (Wilcock et al., 2016) providing
75 observational evidence that caldera floor morphology can be controlled by conjugate fault structures.

76 The proposed caldera collapse models predict considerable differences in the structure of the upper
77 portions of volcanoes that may affect the stress state of the edifice and the movement of magma, resulting
78 in distinct styles of magma recharge and post-collapse volcanism. In this paper we use a dense, active
79 source, seismic tomography study of Santorini caldera (Figure 1) to image the seismic velocity structure of
80 a collapsed caldera at an arc volcano. We interpret the velocity structure in terms of physical properties
81 and then make use of extensive geological studies of the evolution of the volcano and of the latest caldera-
82 forming eruption to explore models that might explain the caldera structure. In addition, we examine how
83 density anomalies beneath the caldera could act to localize present-day magma recharge, specifically in
84 the context of the spatial correlation of caldera structure with a recent episode of volcano inflation.

85 2. Santorini volcano

86 Santorini is an arc volcano in the Hellenic subduction zone (Figure 1) that has been the subject of
87 numerous geological studies over more than a century. In a regional context, Santorini is located within the
88 sedimentary basins and metamorphic horsts of the extended Aegean continental crust. Major explosive
89 activity at Santorini began about 360 ka and included up to 12 large explosive eruptions (Druitt, 2014). It
90 has a history of alternating caldera-forming, explosive, Plinian eruptions and caldera-filling, effusive, shield-
91 building periods. The most recent Plinian event was the explosive Late Bronze Age (LBA) eruption (also
92 known as the Minoan eruption) that formed the present-day caldera 3.6 kyr ago and was followed by
93 effusive dome-building eruptions to create the Kameni islands within the caldera (Figure 2a).

94 The following episodes established the geological setting of the LBA eruption. A large intra-caldera shield
95 edifice, the ~350-m-high Skaros-Therasia complex, was built effusively between 67 and 23 ka (Druitt et al.,
96 1999; Heiken and McCoy, 1984). This shield complex collapsed in the Cape Riva explosive eruption at 22 ka
97 (Fabbro et al., 2013) to form a shallow water caldera located in the northern basin of the present-day
98 caldera (Athanasas et al., 2016). Chemical analysis of the stromatolite lithics show that this caldera was a
99 semi-restricted marine bay with no more than a few meters of water depth (Anadón et al., 2013; Friedrich
100 et al., 1988). Subsequent intra-caldera effusive activity constructed the 2.2-2.5 km³ Pre-Kameni island
101 inferred from black, glassy andesite lavas found throughout the LBA deposits, but not in the present
102 Santorini edifice (Druitt and Francaviglia, 1992; Karátson et al., 2018).

103 Current models for silicic caldera-forming systems involve trans-crustal magmatic systems that evolve
104 significantly over time with rapid final stages of amalgamation preceding the Plinian caldera-forming
105 eruption (Cashman et al., 2017). At Santorini, melt diffusion profiles in orthopyroxene and clinopyroxene
106 crystals from the LBA rhyodacites indicate prolonged storage and segregation of melts in a sub-caldera
107 pluton (8-12 km depth) prior to the LBA eruption (Flaherty, 2018). Since crystals from all eruptive phases
108 yield similar timescales, the authors infer that, on the timescale of a few centuries to years, a shallow (4-6
109 km) short-lived chamber formed that held most of the magma erupted in the LBA eruption.

110 The LBA Plinian eruption occurred in 4 geologically distinct main phases ([Figure 2c](#)) with a total eruption
111 volume between 30 and 80 km³ dense rock equivalent (Bond and Sparks, 1976; Druitt, 2014; Heiken and
112 McCoy, 1984; Johnston et al., 2014; Sparks and Wilson, 1990). The first phase was a Plinian pumice fall
113 indicative of a subaerial eruption. Isopachs of the pumice deposit and the size-distribution of ejected lithics
114 locate the vent on the Pre-Kameni island 1-2 km west of the modern town of Thira (Bond and Sparks, 1976;
115 Druitt and Francaviglia, 1992; Heiken and McCoy, 1984). The second phase is composed of stratified
116 phreatomagmatic base-surge and Plinian deposits showing that variable magma-water interactions

117 occurred at this time (Bond and Sparks, 1976). A higher concentration of lithic blocks in SE Santorini
118 suggests that the vent migrated ~2 km to the SW along a fissure and into the shallow caldera (Heiken and
119 McCoy, 1984; Pfeiffer, 2001).

120 The third phase of the LBA eruption is a massive, weakly stratified, phreatomagmatic ignimbrite. The
121 gradation from well-stratified surge deposits to massive ash-flow deposits (Bond and Sparks, 1976) and low
122 emplacement temperatures (0 to >250°C) inferred from paleomagnetic data (McClelland et al., 1990)
123 reflect increasing water-magma ratios. Deposition of the low-mobility, wet pyroclastic flows beyond the
124 caldera rim suggest that during phase 3 a large tuff-ring (Bond and Sparks, 1976; Sparks and Wilson, 1990)
125 or a mega-tuff cone grew to fill and overtop the existing caldera (~600 m high) (Johnston et al., 2014).
126 Intense magma-water interactions ejected significant lithics up to 10 m in size (Pfeiffer, 2001) including
127 both lavas and tuffs from the caldera floor and black glassy andesites from the Pre-Kameni island (Druitt,
128 2014). Most of the Pre-Kameni island is thought to have been ejected as lithics during this phase (Karátson
129 et al., 2018). The presence of stromatolite clasts and distribution of large lithics around the northern part
130 of the caldera (Friedrich et al., 1988) indicate that a large new vent opened in the northern caldera basin
131 (Pfeiffer, 2001) (Heiken and McCoy, 1984). Pfeiffer (2001) argues that the existing phase 1 and 2 vents may
132 have widened and remained active during this time (Figure 2c).

133 The fourth LBA eruption phase is a voluminous, hot (300-500°C) pyroclastic flow erupted from multiple
134 vents without interaction with water that deposited massive, fine-grained, non-welded ignimbrites in
135 several fans on the coastal plains and in the surrounding sea (Bond and Sparks, 1976; Druitt et al., 1999;
136 Heiken and McCoy, 1984; Sigurdsson et al., 2006; Sparks and Wilson, 1990). The high lithic content in this
137 ignimbrite is considered unusual (Sparks and Wilson, 1990) and the presence of metamorphic basement
138 clasts, especially in the units that erupted first indicate a deeper fragmentation front (Druitt, 2014). These
139 observations point to caldera formation during this last eruption phase that deepened and expanded the
140 existing caldera but remained isolated from the sea (Druitt, 2014; Heiken and McCoy, 1984).

141 After the LBA eruption ended the caldera flooded catastrophically when its NW rim breached (Nomikou
142 et al., 2016a). A number of small-volume intra-caldera eruptions in the last 3.4 kyr built the Kameni islands
143 (Nomikou et al., 2014; Pyle and Elliott, 2006) (Figure 2a). Seismic reflection imaging of intra-caldera fill
144 reveals three units that thicken to fill a depression in the northern caldera basin (Johnston et al., 2015). An
145 upper layer, Unit 1, is on average 20 m thick and consists of modern sediments deposited after the Kameni
146 islands became subaerial. The underlying Unit 2 is about 40-50 m thick and merges with the Kameni
147 volcanics indicating it formed during post-LBA intra-caldera shallow-water phreatomagmatism. Unit 3 is up
148 to 150-200 m thick in the center of the northern caldera basin, and in the southern caldera basin, and is
149 internally faulted. The authors interpret this unit to be downfaulted Minoan pyroclastic deposits that
150 overlie pre-Minoan volcanic basement.

151 Recently, in 2011-2012, Santorini underwent an episode of unrest that included ground inflation
152 consistent with a Mogi source of volume change $\sim 0.02 \text{ km}^3$ at 4.5 km depth (Parks et al., 2015) and seismic
153 swarms on the Kameni lineament (Konstantinou et al., 2013; Papadimitriou et al., 2015) (Figure 2b). The
154 Kolumbo and Kameni lineaments are alignments of volcanic vents and dikes within the Santorini edifice
155 inferred to relate to tectonic extensional stresses and/or structures (Druitt et al., 1999) (Figure 2a) and the
156 Kolumbo line extends from the Santorini volcanic complex toward the nearby Kolumbo seamount (Figure
157 2b).

158 3. Seismic experiment and data

159 Because Santorini's geological evolution and the latest caldera-forming eruption are well understood it
160 is an ideal target for imaging the magmatic system of an arc volcano. We collected a dense, marine-land
161 active source seismic dataset at Santorini volcano in the November-December of 2015. The PROTEUS
162 experiment recorded $\sim 14,300$ controlled-sound sources from the 3600 cubic inch airgun array of the *R/V*
163 *Marcus Langseth* on 90 ocean-bottom and 65 land seismometers and covered an area of $120 \times 60 \text{ km}^2$

164 centered on Santorini (Figure 1). Heath et al. (Tectonism and its relation to magmatism around Santorini
165 volcano from upper crustal P-wave travel time tomography, in prep. for Journal of Geophysical Research)
166 provides a complete description of the experiment, the seismic data, and the tomographic inversion, which
167 we summarize below.

168 The travel time dataset includes over 200,000 first arrival times of crustal refractions (Pg) that were
169 picked first automatically and then manually. Data were picked on either the hydrophone, vertical, or a
170 stack of the hydrophone and vertical channels using a causal 4th order Butterworth filter of 5-25 Hz. Tens
171 of thousands of high signal-to-noise arrivals were picked automatically using `opendTect`
172 (<https://www.dgbes.com>) and were assigned one-sigma errors of 10 msec. One-sigma errors for the
173 manual picks were visually assigned and ranged from 5 to 30 msec. The data set includes travel time arrivals
174 for shots with ranges up to 65 km, with high quality data between 10-30 km at many stations.

175 4. Tomographic inversion and results

176 We obtained a high-resolution seismic image of caldera structure at Santorini using a seismic tomography
177 method to invert first-arriving compressional wave travel times for a P-wave velocity model (Toomey et al.,
178 1994). In this paper we present a 25 km x 25 km x 3 km subset (Figures 3 & 4) of a seismic velocity model
179 that covers the entire domain of the PROTEUS seismic experiment (Heath et al. in prep.).

180 4.1 Inversion

181 Heath et al. (in prep.) inverted the Pg travel time arrivals using a tomographic method that minimizes the
182 prediction error and penalizes the magnitude and roughness of model perturbations (Toomey et al., 1994).
183 The travel times were calculated using a shortest path algorithm (Moser, 1991). The seismic slowness
184 model was gridded at 200 m and extended 125 km x 45 km x 12 km in the horizontal (x parallel to the shot
185 lines) and vertical directions. The slowness model was sheared vertically to include the bathymetry

186 (Toomey et al., 1994) and water wave travel times to the seafloor were calculated on a 50 m by 50 m
187 elevation grid (water velocity = 1.52 km/s). The perturbational grid for the inverse problem was spaced 400
188 m x 400 m x 200 m in the horizontal and vertical directions. New forward travel times are calculated after
189 each iteration of the inverse problem (Toomey et al., 1994). Tens of inversions were conducted to
190 determine the most appropriate inversion parameters. The final model used horizontal and vertical
191 smoothing parameters of 200 and 100, respectively, and a penalty of 1 was used for model perturbations
192 relative to the previous model. Each inversion consisted of 5 model iterations. The model presented here
193 (Figures 3 & 4) was fit to a root mean squared misfit of 15 msec, which corresponds to a χ^2 of 2.2.

194 4.2 Synthetic tomography resolution tests

195 To analyze the resolution of features in the final model we conducted several synthetic tests. First, we
196 superimposed sinusoidal checkerboard anomalies with horizontal wavelengths of 3 km and amplitude
197 ± 0.25 km/s on the 1D velocity structure (Figure S1). For the 1.6 and 2.8 km depth slices, the checkers had
198 vertical wavelengths of 1 km and were centered at 1.6 km depth. Checkers were recovered with amplitudes
199 50-80% of the input values indicating that features of this size are well resolved. We note that the reversal
200 of the sign of the velocity anomaly between 1.6 and 2.8 km depth is well recovered. For the 1.0 km depth
201 slice the checkers had 2 km vertical wavelength and were centered at 1 km depth because the seismic rays
202 average the structure above 1 km; recovery at this depth is 60-80%. Checkers beneath the center of eastern
203 Santorini are not well recovered because of poor coupling of the island seismometers in the LBA ignimbrite
204 deposits. Checkers south of Santorini are not well recovered because the seismic experiment did not
205 sample this area.

206 In the second synthetic test, we superimposed a cylinder with a 1 km/s velocity reduction at the location
207 of the observed caldera low-velocity anomaly (Figure S2). The cylinder had diameter 3 km and height 4 km.
208 Recovery is good down to about 3 km depth below which the recovered the amplitude decreases. The

209 width of the anomaly is reduced because the spatial smoothing constraint cannot capture the abrupt
210 velocity change imposed in the synthetic model. Both resolution tests show that the magnitude of velocity
211 anomalies will be under recovered in the tomographic inversion.

212 4.3. Tomography results

213 The seismic velocity structure of the uppermost crust at Santorini (Figures 3 & 4) reveals a pronounced
214 vertical cylinder of anomalously low velocities within the north basin of the caldera. Low velocities fill most
215 of the upper ~400 m of the topographic caldera and their distribution reflects that of the intra-caldera fill
216 imaged using seismic reflection (Johnston et al., 2015) (Figure 3a & Figure S3). The anomalous low-velocity
217 cylinder lies below this (between 0.5 and 3 km depth) and is narrowly confined compared to the
218 topographic caldera (diameters of 3 km and 10 km, respectively). It is located north of the Kameni islands
219 and lies between the Kolumbo and Kameni lineaments (Figure 2b). The low-velocity anomaly extends down
220 to 3 km depth, has a 3.0 ± 0.5 km diameter and, between 1 and 2 km depth, has a substantial velocity
221 reduction of >2 km/s ($V_P \sim 3.2$ km/s) compared to the surroundings (Figure 4). The velocity-depth gradient
222 below 1 km differs from that of the surrounding metamorphic horsts (Figure 5a); velocities increase very
223 slowly between 1 and 2 km depth, more rapidly from 2 to 2.5 km depth, followed by another gradual
224 increase between 2.5 and 3 km depth ($V_P \sim 5.0 \pm 0.1$ km/s). The low-velocity cylinder is unusual because it
225 underlies only a portion of the caldera floor and has a significant reduction in velocity.

226 The low-velocity cylinder is surrounded by high-velocity rocks (V_P of 5.7 - 6.5 km/s) (Figure 3). At depths
227 less than 2.5 km, the high velocity regions are arc-shaped and contained within the northwest and
228 southeast parts of the topographic caldera - a geometry indicative of solidified intrusives. At deeper depths
229 high velocities extend beyond the caldera and are aligned NE, similar to the orientation of regional horsts
230 of extended basement (Figures 1 & 3d). High velocities beneath southeast Santorini (5.5 km/s at 0.4 and 1
231 km depth) are located where metamorphic basement rocks outcrop at the surface (Figures 2a & 3a&b).
232 Grabens between the associated horsts coincide with low-velocity sedimentary basins (Nomikou et al.,

233 2016b; Piper and Perissoratis, 2003; Tsampouraki-Kraounaki and Sakellariou, 2018) northeast and
234 southwest of the volcano (Figure 3a&b). On the basis of these correlations, we infer that the anomalously
235 high velocities are due to plutonic and metamorphic rocks.

236 5. Calculation of physical properties

237 To understand the subsurface structure of the Santorini caldera we infer physical properties from seismic
238 velocity. Seismic velocities are controlled by various physical properties including composition,
239 temperature, pressure, porosity, and the nature of the pore-filling material. We argue below that the
240 observed low- V_p anomaly between 1 and 2 km depth in the north central caldera is caused by increased
241 porosity filled with hot seawater (Figure 5) and that the alternative where melt fills the pore spaces is
242 unlikely.

243 We estimate the porosity required to explain the observed V_p in the north central caldera by comparing
244 the V_p profile in the caldera to a reference V_p profile for the basement (Figure 5 a & c). We first apply
245 pressure and temperature corrections (Text S1). While we take care to choose appropriate geotherms for
246 the temperature correction, the calculated porosities are far more sensitive to uncertainties in the pore
247 aspect ratio than to uncertainties in the thermal structure (Figure 5). The reference metamorphic profile is
248 generated using a rock of schists and limestones with $V_p = 6.5$ km/s (Christensen and Stanley, 2003) and a
249 background geotherm of 40°C/km. In the caldera, we use a granitic rock with $V_p = 6.2$ km/s (Christensen
250 and Stanley, 2003) and a hotter geotherm estimated from measurements at Santorini and Milos. For the
251 caldera geotherm, the pore fluid we model consists of hot seawater since the temperature remains below
252 370°C.

253 To estimate water-filled porosity we use a self-consistent effective medium approach that treats fluid
254 inclusions as randomly oriented interconnected spheroids (Berryman, 1980). More recent treatments
255 include anisotropy (e.g., Mainprice, 1997) or specific inclusion geometries (Jakobsen et al., 2000; e.g.,

256 Taylor and Singh, 2002) and are more complicated than warranted by our lack of knowledge of the
257 subsurface microstructures. The elastic properties of the pore fluid are calculated for the temperature and
258 pressure of each profile. For the metamorphic reference profile, we assume that the porosity is in the form
259 of cracks with a pore aspect ratio of 0.05 and we obtain a porosity that decreases from 10% at the surface
260 to 2% at 3 km depth (porosities between 1 and 2 km depth decrease from 7% to 3%) (Figure 5b).

261 For the caldera profile, we consider two end-members for the porosity structure of the low-velocity
262 anomaly (Figure 5b & d). In the first case, we assume it consists of tuffs and ignimbrites with a pore aspect
263 ratio of 0.5. This model is an upper bound for the porosity because of the low sensitivity of seismic velocity
264 to relatively equant inclusions. We obtain a porosity of 37% to 27% between 1 and 2 km depth, which is an
265 anomalous porosity relative to the reference profile by 30% to 24%. In the second case, we assume that
266 the low-velocity anomaly is due to fractured igneous rocks with a pore aspect ratio of 0.05. This model
267 provides a lower bound on the porosity because seismic velocity is very sensitive to crack-shaped inclusions.
268 The resulting porosity is 12% to 7% between 1 and 2 km depth - an anomalous porosity relative to the
269 reference profile of 5% to 4%. Using these two end members as bounds, the average anomalous porosity
270 between 1 and 2 km depth ranges from 4 to 28% (Figure 5b).

271 A third geologically motivated structure might have pore aspect ratios that change with depth. One
272 example is labelled 'possible model' in Figure 5b&d and has ignimbrites and tuffs with aspect ratio 0.5 in
273 the upper 750 m transitioning to fractured rocks with aspect ratio 0.05 beneath. The upper layer represents
274 a ~150-m-thick layer of post-LBA deposits overlying a layer of ignimbrites and tuffs that is 200 to 600 m
275 thick on the basis of seismic reflection imaging and geological models (Johnston et al., 2015; 2014). In this
276 upper layer porosities are large, 45%, and the predicted porosity decreases rapidly at the depth where the
277 pore aspect ratio becomes smaller. The unknown subsurface geology makes a range of models with depth-
278 varying pore aspect ratios possible that would lie within the grey field in Figure 5. More accurate constraints

279 on the physical properties and pore geometries can be obtained from joint analysis with shear waves (in
280 particular V_p/V_s ratios), gravity modeling, and drilling within the caldera.

281 Although our preferred interpretation of the low-velocity volume at 1.5 km depth is water porosity at
282 high temperature, a rhyolite or andesite partial melt could also explain the low V_p . In this scenario we would
283 attribute the V_p anomaly to thermal effects up to the solidus and any further reduction of seismic velocity
284 to melt using the same approach as above (Figure S4). We isolate the portion of the V_p anomaly in the
285 caldera that cannot be explained simply with increased temperatures up to the solidus of andesite (800°C).
286 For the pore fluid, we use elastic properties for a silicic partial melt with a bulk modulus of 2.2 GPa and a
287 density of 2300 kg/m³. For melt, we chose pore aspect ratios end-members of 0.05 and 0.2 for grain
288 boundary and triple-junction geometries, respectively. This interpretation predicts melt fractions ranging
289 from 13% to 26% at 1.5 km depth. For average porosities of 10% to 22 % between 1 and 2 km depth, this
290 implies 0.5 to 2.2 km³ of melt assuming a vertical cylindrical volume.

291 While some petrologic and geophysical studies have suggested shallow melt ponding at Santorini
292 (Cottrell et al., 1999; Druitt et al., 2016; Saltogianni et al., 2014), we consider that a large volume of melt
293 at shallow depths is inconsistent with most geological and geophysical observations of the current
294 magmatic system. These observations include that: magma ponding depths of 4-6 km are inferred from
295 melt inclusion saturation pressures for 726 AD Kameni lavas (Druitt, 2014); earthquakes extended to at
296 least 5 km depth during the recent unrest period (Konstantinou et al., 2013; Papadimitriou et al., 2015);
297 and fluxes of magmatic gases and hydrothermal heat within the caldera are relatively low (Papadimitriou
298 et al., 2015; Parks et al., 2013). Consequently, we infer the low-velocity anomaly beneath the north central
299 caldera is caused by a vertical cylindrical volume with a porosity that, between 1 and 2 km depth, is 4-28%
300 higher than the local reference and is filled with high temperature water. This region is likely to be the main
301 hydrothermal reservoir of Santorini (Tassi et al., 2013) and the potential for interaction between rising
302 magma and water in the imaged high-porosity volume is a geo-hazard that needs to be further assessed.

303 6. Discussion

304 The discovery of an anomalous low-velocity, high-porosity vertical cylinder extending from 0.5 to 3 km
305 depth, that is confined to the north central caldera (Figures 3 & 4), is new and was not predicted by existing
306 studies at Santorini. The seismic tomography and reflection data reveal: (i) an inner cylinder of high porosity
307 down to 3 km depth, and (ii) more coherent, down-faulted strata with a maximum thickness of 200 m
308 above the inner cylinder (Johnston et al., 2015).

309 Geological reconstructions of the pre-LBA caldera and its volcanic stratigraphy provide a starting
310 structure that was modified during the LBA eruption and caldera formation (Figure 6a). This includes the
311 remnants of the Skaros-Thirasia lava shields and their hyaloclastite cores that collapsed during the Cape
312 Riva eruption to form the shallow pre-LBA caldera (Sparks and Wilson, 1990). We estimate a thickness of
313 400-600 m on the basis of the inferred 350-m elevation of the Skaros lava shield summit (Druitt et al., 1999;
314 Heiken and McCoy, 1984). After the Cape Riva eruption and prior to the LBA eruption the Pre-Kameni island
315 was built of black, glassy andesites and may also have had a hyaloclastite core. Most of the Pre-Kameni
316 island is thought to have been ejected as lithics during the LBA eruption (Karátson et al., 2018). The primary
317 low-velocity anomaly recovered in this study lies at 1-2 km depth and is located below these pre-existing
318 deposits (Figure 6a).

319 The imaged low-velocity anomaly also lies between the Kolumbo and Kameni lineaments (KL2 and KL1,
320 respectively in Figure 6a). These volcanic alignments appear to be long-lived since numerous dikes lie
321 parallel to the down-dropped graben of the Kolumbo line (Browning et al., 2015) and since earlier volcanic
322 vents, both for intra-caldera effusive and Plinian explosive eruptions, lie near the Kameni line (Figure 2
323 a&b). These correlations suggest that the low-density column may have existed prior to the LBA event and
324 be long-lived; to reflect this uncertainty we show it with a question mark in Figure 6a.

325 The observed seismic velocity structure correlates with the four phases of the LBA eruption as follows.
326 The initial phase 1 and phase 2 vents (Druitt, 2014; Heiken and McCoy, 1984; Pfeiffer, 2001) are associated
327 with the southeast boundary of the low-velocity cylinder (Figure 2c). The phase 3 vent is reconstructed
328 within the shallow-water north caldera basin (Heiken and McCoy, 1984; Pfeiffer, 2001) approximately along
329 the northern margin of the low-velocity cylinder (Figure 2c). Geological observations of several ignimbrite
330 fans distributed around the caldera (Bond and Sparks, 1976; Druitt, 2014; Heiken and McCoy, 1984) and a
331 diverse lithology of ejected rock debris (Druitt and Francaviglia, 1992) indicate that the entire topographic
332 caldera subsided during phase 4 and we observe high velocities beneath the remainder of the caldera floor
333 (Figure 3a-c). We argue that this last observation implies that the formation of the topographic caldera
334 occurred by coherent down-drop of the larger caldera during the last phase of the LBA eruption (Figure 6c).

335 Below we explore three possible end-member models for the formation of the inner seismic low-velocity
336 anomaly (Figure 6b,d-f); the first two are motivated by the geological observations of the LBA eruption of
337 Santorini, while the third is a general sequence for caldera formation.

338 6.1 Collapsed plug filled with volcanic deposits

339 In the first scenario, the low-velocity cylinder is filled with tuffs and ignimbrite products (Figure 6d) and
340 the average porosity between 1 and 2 km depth is high, ~32%. This interpretation requires extensive
341 foundering of the low-velocity plug and infilling with eruptive products and is similar to that proposed for
342 the larger Valles caldera (Lipman, 1997). Foundering and filling of this space may have happened entirely
343 during the LBA eruption, in which case pre-existing rock 3 km wide and at least 2 km deep (a cylindrical
344 volume of 14 km³) subsided into the collapsing magmatic system - an interpretation that is compatible with
345 the volume erupted during LBA phases 1 to 3 (14 to 20 km³ dense rock equivalent excluding the lithics
346 (Karátson et al., 2018)). The correlation of the Kolumbo and Kameni lineaments with the margins of the
347 low-velocity plug, suggests that these structural weaknesses could have facilitated large-scale foundering
348 of the region between them, accompanied by deposition of phreatomagmatic and pyroclastic products in

349 the generated space. The inference that a tuff ring or mega-tuff cone ~600 m tall grew within the caldera
350 during phase 3 of the LBA eruption (Johnston et al., 2014) implies that the plug may have dropped at the
351 end of phase 3 with a majority of the tuff products collapsing into it – in which case the stratigraphic layering
352 observed in Unit 3 of the seismic reflection images of the LBA deposits within the caldera (Johnston et al.,
353 2015) would correspond to overlying phase 4 ignimbrites .

354 Alternatively, the spatial association of earlier volcanic vents (Druitt et al., 1999) with the low-velocity
355 cylinder, suggests that a tuff/ignimbrite-filled plug may have formed by repeated foundering and infilling
356 of the same region over multiple eruptive cycles at Santorini. This interpretation is consistent with the
357 apparent longevity of the Kolumbo and Kameni lines. In this case, a lesser degree of foundering is needed
358 during the LBA eruption and the structure is built up gradually. A further implication is that the margins of
359 this pre-existing structure then provided pathways for, and localized, LBA vent formation during phases 1
360 through 3.

361 6.2 Phreatomagmatic rock breakup

362 Another possibility is that the high-porosity cylinder formed by rock breakup during the intensely
363 phreatomagmatic phase 3 of the LBA eruption making a large diatreme-like structure ([Figure 6e](#)) (Escher,
364 1929; Sparks and Wilson, 1990). In this scenario, porosity is dominated by fractures and an average porosity
365 of 9% between 1 and 2 km depth is inferred. Reaming and rock excavation undoubtedly took place given
366 the energy required to eject up to 10-m-diameter lithics during phase 3 (Pfeiffer, 2001). The diatreme may
367 also be the origin of the large tuff-ring proposed to explain deposition of phase 3 flows on the caldera rim
368 (Sparks and Wilson, 1990). While analogue models of diatremes show that the ejected lithics are usually
369 sourced from only a few 100 meters below the surface, it is possible that rock breakup from the powerful
370 phreatomagmatic explosions as well as water penetration contributed to fracturing as deep as 2 km
371 (Valentine et al., 2014). We consider this scenario less likely because the observed seismic anomaly (3 km

372 wide at 1.5 km depth) is larger in spatial extent and depth than the largest studied diatremes, which are 2
373 km wide and 2 km deep and narrow with depth (White and Ross, 2011).

374 However, this scenario has features that fit both the geology and the subsurface structure and more
375 study is needed to investigate energy partitioning during large phreatomagmatic eruptions. For example,
376 it is not clear how energy is divided between launching of material and sound waves into the atmosphere
377 versus the passage of shock waves within the underlying rock, hence the spatial extent of hydrofracturing
378 or damage is poorly constrained. Numerical simulations of rock damage by underground explosions suggest
379 that damage extends well away from the cavity (e.g., Johnson and Sammis, 2001) and is more extensive
380 below than above the explosion site (Ma et al., 2011). In addition, post-explosion well-logging studies reveal
381 that explosions that are high in gaseous products or within water-filled media generate more extensive
382 macro-fractures (Stroujkova, 2018). Furthermore, studies of the mechanisms of deep-sea explosive
383 eruptions show that, because the super-critical behavior of seawater is significantly different from that of
384 fresh water, a vapor phase exists at super-critical pressures that is hydrodynamically unstable and results
385 in explosive behavior at high pressures if the magma-water ratios and mixing mechanisms are right
386 (Wohletz, 2003). Further understanding requires modeling of the accumulated damage pattern from
387 repeated phreatomagmatic explosions and their spatial and depth extent given the inferred vent geometry
388 and the fragmentation depth of phase 2 and 3 erupted products.

389 6.3 Multistage, nested caldera collapse

390 Our final scenario seeks to put the formation of both the intra-caldera, cylindrical, low-velocity region
391 and the topographic caldera in a framework of evolving caldera deformation as magma continues to be
392 withdrawn over the course of an eruption. In stage A of this scenario, chaotic collapse of the area between
393 the phase 1, 2 and 3 vents occurred forming the high-porosity cylinder in the northern caldera (Figure 6f).
394 We again speculate that either the vents formed along the Kolumbo and Kameni lines, and consequently
395 the area between them collapsed, or that the cylindrical structure already existed and the LBA vents again

396 formed along its boundaries during collapse (Figure 6f). Analogue studies show that instabilities during
397 down drop of a 3D plug can cause vent location and eruptive products to vary dramatically during
398 subsidence (Kennedy et al., 2008), potentially explaining the temporal migration of vent locations during
399 phases 1 through 3 and the variations in eruptive products during individual eruptive phases.

400 In the generalized caldera collapse models, the inner stage A involves breakup of the volume overlying
401 the evacuating magma system by a number of reverse faults propagating upward (Figure 6f) (Roche et al.,
402 2000; Scandone, 1990; Scandone and Acocella, 2007). If the volume between 1 and 2 km depth is
403 dominated by fractured rock, the porosity is ~10%. If larger collapse blocks contribute more equant
404 fractures the required porosity would be higher (Figure 5). Phase 4 ignimbrites likely fill the upper portion
405 of the low-velocity collapse cylinder (Johnston et al., 2015) and the inferred porosity for a model where
406 aspect ratio decreases with depth is illustrated in Figure 5. Alternatively, porosity may be higher from 1 to
407 2 km depth because of more intense brecciation below a transverse arch that develops within the collapsing
408 column and acts to support the overlying material (Holohan et al., 2015; Scandone, 1990) (Figure 6f).

409 In stage B of this caldera formation scenario, the observation of high velocities beneath the remainder of
410 the caldera (Figures 3 & 4) suggests that coherent subsidence of the entire topographic caldera to ~500 m
411 below sea level occurred during phase 4 of the eruption (Figures 6c). Resolved high velocities within the
412 broader caldera could reflect down-dropped Skaros-Thirasia shield lavas in the upper 500 m and/or igneous
413 rocks along the caldera edges {Sakellariou:2012tf}.

414 In this scenario, the seismic and geological results from Santorini provide observational evidence for
415 models of multistage, nested caldera formation during progressive caldera subsidence (Acocella, 2006).
416 During stage A, the inner collapse column would be formed along outward-dipping reverse faults with
417 breakup of the roof rock (Figure 6g). During stage B, a new outer ring of collapse would cause subsidence
418 of the entire topographic caldera and the opening of new vents during phase 4 (Figure 6d). Accordingly,

419 the geologically distinctive LBA eruptive phases form as a direct result of geological processes occurring
420 during each stage of caldera formation (Figure 6).

421 It is quite possible that all three of the above scenarios (Figure 6 e-g) play a role in generating the inner
422 cylinder of high porosities at Santorini. Thus, rock breakup by reverse faulting during inner caldera collapse
423 may be accompanied by, or even promoted by, fracturing and reaming of the volcanic vent during violent
424 magma-water interactions. In addition, the upper portions of the high-porosity cylinder are probably
425 formed by the deposition of eruptive volcanic products including tuffs, pyroclasts, and ignimbrites.

426 6.4 Present day magma recharge

427 The spatial correlation of post-collapse volcanism with the upper-crustal low-velocity volume suggests
428 that present-day accumulation of magma in the upper ~5 km of the crust may be focused beneath the low-
429 density column due to edifice stresses generated by both the low-density cylinder and the caldera
430 topography (Figure 7). Since the 2011-2012 magmatic inflation episode (Parks et al., 2015) occurred directly
431 beneath the low-velocity cylinder (Figure 2b), we suggest that a low-density cylinder within the caldera
432 affects the dynamics of the underlying magmatic system. Previous authors have demonstrated that magma
433 emplacement in the upper crust is influenced by stresses within the volcanic edifice due to topographic
434 loads (Corbi et al., 2015; Muller et al., 2001; Pinel et al., 2017) and internal structure (Gudmundsson, 1990;
435 Karlstrom et al., 2009). Finite element calculations of edifice stress (Corbi et al., 2015) also show that
436 volcano unloading caused by the topographic depression associated with caldera formation favors sill
437 emplacement beneath the caldera floor because the least compressive stress becomes vertical. A low-
438 density cylinder would unload the volcano in a similar way to caldera formation.

439 The relative importance of unloading by a low-density anomaly compared to that by caldera formation
440 can be estimated from the lithostatic pressure at 4 km below sea level (Figure 7). We sum the contributions
441 of the topography, the water column, and the crustal density calculated from seismic velocity using the

442 relationships of Brocher (2005) at each grid point (Figure 7b-d). The predicted total lithostatic pressure
443 varies from 85 to 120 MPa (Figure 7b) and has a minimum coincident with the seismic low-velocity anomaly.
444 The topography of the volcanic edifice and the surrounding sea contribute variations of ~20 MPa to
445 gravitational loading with a broad minimum throughout the caldera except beneath the Kameni islands
446 (Figure 7c). The calculated differences in gravitational load due to density variations within the upper crust
447 are ~14 MPa and have a pronounced low beneath the low-velocity anomaly (Figure 7d). While complete
448 exploration of this idea requires modeling of edifice stresses, gravitational loading from internal density
449 variations is likely to be important since the magnitude is comparable to that from topography (Figure
450 7c&d). The correlation of older volcanic vents with the low-velocity anomaly further suggests that a
451 feedback between the internal structure of the volcanic edifice and localization of magma emplacement in
452 the upper crust may have occurred through several eruptive cycles at Santorini. Such a feedback would
453 result in long-lived and actively, self-organized, centralized magmatic activity.

454 7. Conclusions

455 To understand caldera formation mechanisms at arc volcanoes we present a P-wave seismic velocity
456 model of the upper crust at Santorini in the Hellenic volcanic arc of Greece. We find a low-velocity anomaly
457 in the upper 3 km with diameter of 3 ± 0.5 km that is confined beneath the north-central portion of the
458 caldera. We infer that this represents a volume of excess porosity of 4 to 28% filled with hot seawater and
459 argue that the alternative explanation of melt filling the pore spaces is unlikely. The Kolumbo and Kameni
460 lineaments bound the margins of the anomaly and the locations of the vents for the first three phases of
461 the Late Bronze Age eruption correlate with the imaged structure.

462 We combine our results with previous geological studies to infer that collapse of a limited area of the
463 caldera floor resulted in a high-porosity, low-density cylindrical volume, which formed by either chaotic
464 collapse along reverse faults, wholesale subsidence and infilling with tuffs and ignimbrites,

465 phreatomagmatic fracturing, or a combination of these processes. Phase 4 eruptive vents are located
466 along the margins of the topographic caldera and the velocity structure indicates that coherent down-
467 drop of the wider topographic caldera followed more limited collapse in the northern caldera. This
468 progressive collapse sequence is consistent with models for multi-stage formation of nested calderas
469 along conjugate reverse and normal faults. If this model holds, each stage of caldera formation could
470 produce the geologically distinctive eruptive phases of the LBA eruption.

471 The pressure source of edifice inflation during 2011-2012 unrest lies at ~ 4.5 km, directly beneath this
472 cylindrical low-density anomaly, and we hypothesize that sub-surface density anomalies influence
473 present-day magma recharge. The correlation of older volcanic vents with the low-velocity anomaly
474 further suggests that this conduit vent system may be long-lived. We postulate that past collapse
475 mechanisms at Santorini influence magma focusing between eruptive cycles, an actively self-organized
476 feedback process that may be important in other volcanoes.

477 Acknowledgements

478 We thank the officers, crew, and marine management office of the *R/V Marcus G. Langseth* as well as
479 the OBS teams from Scripps Institution of Oceanography and Woods Hole Oceanographic Institution and
480 their staff for their role in the data collection. Additional assistance was provided by onboard passive
481 acoustic technicians and marine mammal observers to ensure that data collection was accomplished in
482 compliance with guidelines set forth by marine environmental assessments and permits. The Greek military
483 provided helicopter support for seismometer installation on the smaller islands. We thank Tim Druitt,
484 Thomas Giachetti, Gene Humphreys, Stephen Sparks, Amanda Thomas, and Josef Dufek for helpful
485 discussions and/or reviews. The experiment and analysis were supported by the National Science
486 Foundation under grant number OCE-1459794 to the University of Oregon and Leverhulme Grant RPG-
487 2015-363 to Imperial College London.

488 Author contributions

489 E.E.E.H. wrote the manuscript with comments from the co-authors and drafted all the figures except
490 Figures 4 & 5. All authors discussed the results and their implications and assisted in revising the
491 manuscript. B.A.H. performed the data picking and tomographic analysis and drafted Figure 4; E.E.E.H. and
492 D.R.T. supervised the project. M.P. performed the calculation of physical properties and drafted Figure 5.
493 E.E.E.H., D.R.T, J.V.M, C.B.P. P.N., and M.W. designed, funded, permitted, and executed the data collection.

494 References

- 495 Acocella, V., 2006. Caldera types: How end-members relate to evolutionary stages of collapse. *Geophys. Res.*
496 *Lett* 33, L18314. doi:10.1029/2006GL027434
- 497 Anadón, P., Canet, C., Friedrich, W.L., 2013. Aragonite stromatolitic buildups from Santorini (Aegean Sea,
498 Greece): Geochemical and palaeontological constraints of the caldera palaeoenvironment prior to the
499 Minoan eruption (ca 3600 yr bp). *Sedimentology* 60, 1128–1155. doi:10.1111/sed.12025
- 500 Aramaki, S., 1984. Formation of the Aira Caldera, southern Kyushu, ~22,000 years ago. *Journal of Geophysical*
501 *Research: Solid Earth* (1978–2012) 89, 8485–8501. doi:10.1029/JB089iB10p08485
- 502 Athanassas, C.D., Bourlès, D.L., Braucher, R., Druitt, T.H., Nomikou, P., Léanni, L., 2016. Evidence from cosmic
503 ray exposure (CRE) dating for the existence of a pre-Minoan caldera on Santorini, Greece. *Bull. Volc.* 78, 1–
504 13. doi:10.1007/s00445-016-1026-3
- 505 Beachly, M.W., Hooft, E.E.E., Toomey, D.R., Waite, G.P., 2012. Upper crustal structure of Newberry Volcano
506 from P-wave tomography and finite difference waveform modeling. *J. Geophys. Res.* 117, B10311.
507 doi:10.1029/2012JB009458
- 508 Berryman, J.G., 1980. Long-wavelength propagation in composite elastic media I. Spherical inclusions. *J.*
509 *Acoust. Soc. Am.* 68, 1809–1819. doi:10.1121/1.385172
- 510 Bond, A., Sparks, R.S.J., 1976. The Minoan eruption of Santorini, Greece. *J. Geol. Soc.* 132, 1–16.
511 doi:10.1144/gsjgs.132.1.0001
- 512 Brocher, T.M., 2005. Empirical relations between elastic wavespeeds and density in the Earth's crust. *Bull.*
513 *Seismol. Soc. Amer.* 95, 2081–2092. doi:10.1785/0120050077
- 514 Browning, J., Drymoni, K., Gudmundsson, A., 2015. Forecasting magma-chamber rupture at Santorini volcano,
515 Greece. *Sci. Rep.* 5, 15785. doi:10.1038/srep15785
- 516 Cashman, K.V., Sparks, R.S.J., Blundy, J.D., 2017. Vertically extensive and unstable magmatic systems: A unified
517 view of igneous processes. *Science* 355, eaag3055. doi:10.1126/science.aag3055
- 518 Christensen, N.I., Stanley, D., 2003. Seismic velocities and densities of rocks. *International Handbook of*
519 *Earthquake and Engineering Seismology* 81, 1587–1594.

- 520 Corbi, F., Rivalta, E., Pinel, V., Maccaferri, F., Bagnardi, M., Acocella, V., 2015. How caldera collapse shapes the
521 shallow emplacement and transfer of magma in active volcanoes. *Earth Planet. Sci. Lett.* 431, 287–293.
522 doi:10.1016/j.epsl.2015.09.028
- 523 Cottrell, E., Gardner, J.E., Rutherford, M.J., 1999. Petrologic and experimental evidence for the movement and
524 heating of the pre-eruptive Minoan rhyodacite (Santorini, Greece). *Contrib. Mineral. Petrol.* 135, 315–331.
525 doi:10.1007/s004100050514
- 526 Deplus, C., Bonvalot, S., Dahrin, D., Diamant, M., Harjono, H., Dubois, J., 1995. Inner structure of the Krakatau
527 volcanic complex (Indonesia) from gravity and bathymetry data. *J. Volc. Geotherm. Res.* 64, 23–52.
528 doi:10.1016/0377-0273(94)00038-I
- 529 Druitt, T.H., 2014. New insights into the initiation and venting of the Bronze-Age eruption of Santorini
530 (Greece), from component analysis. *Bull. Volc.* 76, 794. doi:10.1007/s00445-014-0794-x
- 531 Druitt, T.H., Edwards, L., Mellors, R.M., Pyle, D.M., Sparks, R.S.J., Lanphere, M., Davies, M., Barreiro, B., 1999.
532 Santorini volcano. *Geol. Soc. Lond. Mem* 19, 165pp.
- 533 Druitt, T.H., Francaviglia, V., 1992. Caldera formation on Santorini and the physiography of the islands in the
534 late Bronze Age. *Bull. Volcanol.* 54, 484–493. doi:10.1007/BF00301394
- 535 Druitt, T.H., Mercier, M., Florentin, L., Deloule, E., Cluzel, N., Flaherty, T., Me dard, E., Cadoux, A., 2016.
536 Magma storage and extraction associated with Plinian and Interplinian activity at Santorini caldera
537 (Greece). *Journal of Petrology* 57, 461–494. doi:10.1093/petrology/egw015
- 538 Escher, B.G., 1929. On the formation of calderas. *Leidsche Geologische Mededelingen* 3, 183–219.
- 539 Fabbro, G.N., Druitt, T.H., Scaillet, S., 2013. Evolution of the crustal magma plumbing system during the build-
540 up to the 22-ka caldera-forming eruption of Santorini (Greece). *Bull. Volc.* 75, 1–22. doi:10.1007/s00445-
541 013-0767-5
- 542 Farrell, J., Smith, R.B., Husen, S., Diehl, T., 2015. Tomography from 26 years of seismicity revealing that the
543 spatial extent of the Yellowstone crustal magma reservoir extends well beyond the Yellowstone caldera.
544 *Geophys. Res. Lett* 41, 3068–3073. doi:10.1002/(ISSN)1944-8007

545 Flaherty, T., 2018. Multiple timescale constraints for high-flux magma chamber assembly prior to the Late
546 Bronze Age eruption of Santorini (Greece). *Contrib. Mineral. Petrol.* 173, 75. doi:10.1007/s00410-018-
547 1490-1

548 Friedrich, W.L., Eriksen, U., Tauber, H., Heinemeier, J., Rud, N., Thomsen, M.S., Buchardt, B., 1988. Existence of
549 a water-filled caldera prior to the Minoan eruption of Santorini, Greece. *Naturwissenschaften* 75, 567–
550 569. doi:10.1007/BF00377720

551 Gudmundsson, A., 1990. Emplacement of dikes, sills and crustal magma chambers at divergent plate
552 boundaries. *Tectonophys.* 176, 257–275. doi:10.1016/0040-1951(90)90073-H

553 Gudmundsson, M.T., Jónsdóttir, K., Hooper, A., Holohan, E.P., Halldórsson, S.A., Ófeigsson, B.G., Cesca, S.,
554 Vogfjörð, K.S., Sigmundsson, F., Högnadóttir, T., Einarsson, P., Sigmarsson, O., Jarosch, A.H., Jónasson, K.,
555 Magnússon, E., Hreinsdóttir, S., Bagnardi, M., Parks, M.M., Hjörleifsdóttir, V., Pálsson, F., Walter, T.R.,
556 Schöpfer, M.P.J., Heimann, S., Reynolds, H.I., Dumont, S., Bali, E., Gudfinnsson, G.H., Dahm, T., Roberts,
557 M.J., Hensch, M., Belart, J.M.C., Spaans, K., Jakobsson, S., Gudmundsson, G.B., Fridriksdóttir, H.M., Drouin,
558 V., Dürig, T., Aðalgeirsdóttir, G., Riishuus, M.S., Pedersen, G.B.M., van Boeckel, T., Oddsson, B., Pfeffer,
559 M.A., Barsotti, S., Bergsson, B., Donovan, A., Burton, M.R., Aiuppa, A., 2016. Gradual caldera collapse at
560 Bárdarbunga volcano, Iceland, regulated by lateral magma outflow. *Science* 353, aaf8988–8.
561 doi:10.1126/science.aaf8988

562 Heath, B.A., Hooft, E.E.E., Toomey, D.R., Bezada, M.J., 2015. Imaging the magmatic system of Newberry
563 Volcano using joint active source and teleseismic tomography. *Geochem. Geophys. Geosyst.* 16, 4433–
564 4448. doi:10.1002/2015GC006129

565 Heiken, G., McCoy, F., 1984. Caldera development during the Minoan eruption, Thira, Cyclades, Greece. *J.*
566 *Geophys. Res.* 89, 8441–8462. doi:10.1029/JB089iB10p08441

567 Holohan, E.P., Schöpfer, M.P.J., Walsh, J.J., 2015. *Earth and Planetary Science Letters.* *Earth Planet. Sci. Lett.*
568 421, 139–151. doi:10.1016/j.epsl.2015.03.003

569 Hooft, E.E.E., Nomikou, P., Toomey, D.R., Lampridou, D., Getz, C., Christopoulou, M.-E., O'Hara, D., Arnoux,
570 G.M., Bodmer, M., Gray, M., Heath, B.A., VanderBeek, B.P., 2017. Backarc tectonism, volcanism, and mass
571 wasting shape seafloor morphology in the Santorini-Christiana-Amorgos region of the Hellenic Volcanic
572 Arc. *Tectonophys.* 712-713, 396–414. doi:10.1016/j.tecto.2017.06.005

- 573 Jakobsen, M., Hudson, J.A., Minshull, T.A., Singh, S.C., 2000. Elastic properties of hydrate-bearing sediments
574 using effective medium theory. *J. Geophys. Res.* 105, 561–577. doi:10.1029/1999JB900190
- 575 Johnson, L.R., Sammis, C.G., 2001. Effects of Rock Damage on Seismic Waves Generated by Explosions. *Pure*
576 *Appl Geophys* 158, 1869–1908. doi:10.1007/PL00001136
- 577 Johnston, E.N., Sparks, R.S.J., Nomikou, P., Livanos, I., Carey, S., Phillips, J.C., Sigurdsson, H., 2015. Stratigraphic
578 relations of Santorini's intracaldera fill and implications for the rate of post-caldera volcanism. *J. Geol. Soc.*
579 *Lon.* 172, 323–335. doi:10.1144/jgs2013-114
- 580 Johnston, E.N., Sparks, R.S.J., Phillips, J.C., Carey, S., 2014. Revised estimates for the volume of the Late Bronze
581 Age Minoan eruption, Santorini, Greece. *J. Geol. Soc.* 171, 583–590. doi:10.1144/jgs2013-113
- 582 Karátson, D., Gertisser, R., Telbisz, T., Vereb, V., Quidelleur, X., Druitt, T., Nomikou, P., Kósik, S., 2018. Towards
583 reconstruction of the lost Late Bronze Age intra-caldera island of Santorini, Greece. *Sci. Rep.* 8, 548.
584 doi:10.1038/s41598-018-25301-2
- 585 Karlstrom, L., Dufek, J., Manga, M., 2009. Organization of volcanic plumbing through magmatic lensing by
586 magma chambers and volcanic loads. *J. Geophys. Res.* 114, 937. doi:10.1029/2009JB006339
- 587 Kennedy, B.M., Mark Jellinek, A., Stix, J., 2008. Coupled caldera subsidence and stirring inferred from analogue
588 models. *Nature Geosci.* 1, 385–389. doi:10.1038/ngeo206
- 589 Konstantinou, K.I., Evangelidis, C.P., Liang, W.T., Melis, N.S., Kalogeras, I., 2013. Seismicity, Vp/Vs and shear
590 wave anisotropy variations during the 2011 unrest at Santorini caldera, southern Aegean. *J. Volc.*
591 *Geotherm. Res.* 267, 57–67. doi:10.1016/j.jvolgeores.2013.10.001
- 592 Lipman, P.W., 1997. Subsidence of ash-flow calderas: relation to caldera size and magma-chamber geometry.
593 *Bull. Volc.* 59, 198–218. doi:10.1007/s004450050186
- 594 Ma, G.W., Hao, H., Wang, F., 2011. Simulations of explosion-induced damage to underground rock chambers.
595 *Journal of Rock Mechanics and Geotechnical Engineering* 3, 19–29. doi:10.3724/SP.J.1235.2011.00019
- 596 Mainprice, D., 1997. Modeling the anisotropic seismic properties of partially molten rocks found at mid-ocean
597 ridges. *Tectonophys.* 279, 161–179.

598 McClelland, E., Thomas, R., Hardy, D.A., 1990. A palaeomagnetic study of Minoan age tephra from Thera, in:
599 Thera and the Aegean World Iii, Proceedings of the Third International Congress. The Thera Foundation,
600 pp. 129–138.

601 Moser, T.J., 1991. Shortest path calculation of seismic rays. *Geophysics* 56, 59–67. doi:10.1190/1.1442958

602 Muller, J.R., Ito, G., Martel, S.J., 2001. Effects of volcano loading on dike propagation in an elastic half-space. *J.*
603 *Geophys. Res.* 106, 11101–11113. doi:10.1029/2000JB900461

604 Nomikou, P., Druitt, T.H., Hubscher, C., Mather, T.A., Paulatto, M., Kalnins, L.M., Kelfoun, K., Papanikolaou, D.,
605 Bejelou, K., Lampridou, D., Pyle, D.M., Carey, S., Watts, A.B., Weiß, B., Parks, M.M., 2016a. Post-eruptive
606 flooding of Santorini caldera (Greece), and implications for tsunami generation. *Nature Comm.* 7, 1–22.
607 doi:10.1038/ncomms13

608 Nomikou, P., Hübscher, C., Ruhnau, M., Bejelou, K., 2016b. Tectono-stratigraphic evolution through successive
609 extensional events of the Anydros Basin, hosting Kolumbo volcanic field at the Aegean Sea, Greece.
610 *Tectonophys.* 671, 202–217. doi:10.1016/j.tecto.2016.01.021

611 Nomikou, P., Parks, M.M., papanikolaou, D., Pyle, D.M., Mather, T.A., Carey, S., Watts, A.B., Paulatto, M.,
612 Kalnins, M.L., Livanos, I., Bejelou, K., Simou, E., Perros, I., 2014. The emergence and growth of a submarine
613 volcano: The Kameni islands, Santorini (Greece). *GeoResJ* 1-2, 8–18. doi:10.1016/j.grj.2014.02.002

614 Papadimitriou, P., Kapetanidis, V., Karakonstantis, A., Kaviris, G., Voulgaris, N., Makropoulos, K., 2015. The
615 Santorini Volcanic Complex: A detailed multi-parameter seismological approach with emphasis on the
616 2011–2012 unrest period. *J. Geodynamics* 85, 32–57. doi:10.1016/j.jog.2014.12.004

617 Parks, M.M., Caliro, S., Chiodini, G., Pyle, D.M., Mather, T.A., Berlo, K., Edmonds, M., Biggs, J., Nomikou, P.,
618 Raptakis, C., 2013. Distinguishing contributions to diffuse CO₂ emissions in volcanic areas from magmatic
619 degassing and thermal decarbonation using soil gas ²²²Rn–^δ13C systematics: Application to Santorini
620 volcano, Greece. *Earth Planet. Sci. Lett.* 377–378, 180–190. doi:10.1016/j.epsl.2013.06.046

621 Parks, M.M., Moore, J., Papanikolaou, X., 2015. From quiescence to unrest: 20 years of satellite geodetic
622 measurements at Santorini volcano, Greece. *J. Geophys. Res.* 120, doi: 10.1002–(ISSN)2169–9356.
623 doi:10.1002/(ISSN)2169-9356

624 Pfeiffer, T., 2001. Vent development during the Minoan eruption (1640 BC) of Santorini, Greece, as suggested
625 by ballistic blocks. *J. Volc. Geotherm. Res.* 106, 229–242. doi:10.1016/S0377-0273(00)00273-0

- 626 Pinel, V., Carrara, A., Maccaferri, F., Rivalta, E., Corbi, F., 2017. A two-step model for dynamical dike
627 propagation in two dimensions: Application to the July 2001 Etna eruption. *J. Geophys. Res.* 122, 1107–
628 1125. doi:10.1002/2016JB013630
- 629 Piper, D.J.W., Perissoratis, C., 2003. Quaternary neotectonics of the South Aegean arc. *Marine Geol.* 198, 259–
630 288. doi:10.1016/S0025-3227(03)00118-X
- 631 Pyle, D.M., Elliott, J.R., 2006. Quantitative morphology, recent evolution, and future activity of the Kameni
632 Islands volcano, Santorini, Greece. *Geosphere* 2, 253. doi:10.1130/GES00028.1
- 633 Roche, O., Druitt, T.H., Merle, O., 2000. Experimental study of caldera formation. *J. Geophys. Res.* 105, 395–
634 416. doi:10.1029/1999JB900298
- 635 Saltogianni, V., Stiros, S.C., Newman, A.V., Flanagan, K., Moschas, F., 2014. Time-space modeling of the
636 dynamics of Santorini volcano (Greece) during the 2011–2012 unrest. *J. Geophys. Res.*
637 doi:10.1002/2014JB011409
- 638 Scandone, R., 1990. Chaotic collapse of calderas. *J. Volc. Geotherm. Res.* 42, 285–302. doi:10.1016/0377-
639 0273(90)90005-Z
- 640 Scandone, R., Acocella, V., 2007. Control of the aspect ratio of the chamber roof on caldera formation during
641 silicic eruptions. *Geophys. Res. Lett.* 34, L18314–4. doi:10.1029/2007GL032059
- 642 Sigurdsson, H., Carey, S., Alexandri, M., 2006. Marine investigations of Greece's Santorini volcanic field. *EOS*
643 (Trans. Am. Geophys. Un.) 87, 337–348.
- 644 Sparks, R., Wilson, C., 1990. The Minoan deposits: a review of their characteristics and interpretation, in: Thera
645 and the Aegean World Iii, Proceedings of the Third International Congress. The Thera Foundation, pp. 89–
646 99.
- 647 Stroujkova, A., 2018. Rock Damage and Seismic Radiation: A Case Study of the Chemical Explosions in New
648 Hampshire. *Bull. Seismol. Soc. Amer.* 1–14. doi:10.1785/0120180117
- 649 Tassi, F., Vaselli, O., Papazachos, C.B., (null), L.G., Chiodini, G., Vougioukalakis, G.E., Karagianni, E., Vamvakaris,
650 D., Panagiotopoulos, D., 2013. Geochemical and isotopic changes in the fumarolic and submerged gas
651 discharges during the 2011–2012 unrest at Santorini caldera (Greece). *Bull. Volc.* 75, 15.
652 doi:10.1007/s00445-013-0711-8

- 653 Taylor, M., Singh, S.C., 2002. Composition and microstructure of magma bodies from effective medium theory.
654 Geophysical Journal International 149, 15–21. doi:10.1046/j.1365-246X.2002.01577.x
- 655 Toomey, D.R., Solomon, S.C., Purdy, G.M., 1994. Tomographic imaging of the shallow crustal structure of the
656 East Pacific Rise at 9 30'N. J. Geophys. Res. 99, 24–24. doi:10.1029/94JB01942
- 657 Tsampouraki-Kraounaki, K., Sakellariou, D., 2018. Seismic stratigraphy and geodynamic evolution of Christiana
658 Basin, South Aegean Arc. Marine Geol. 399, 135–147. doi:10.1016/j.margeo.2018.02.012
- 659 Valentine, G.A., Graettinger, A.H., Sonder, I., 2014. Explosion depths for phreatomagmatic eruptions. Geophys.
660 Res. Lett 41, 3045–3051. doi:10.1002/2014GL060096
- 661 Vanorio, T., 2005. Three-dimensional seismic tomography from Pwave and Swave microearthquake travel
662 times and rock physics characterization of the Campi Flegrei Caldera. J. Geophys. Res. 110, 139.
663 doi:10.1111/j.1365-246X.1980.tb02612.x
- 664 Walker, G.P.L., 1984. Downsag calderas, ring faults, caldera sizes, and incremental caldera growth. J. Geophys.
665 Res. 89, 8407–8416. doi:10.1029/JB089iB10p08407
- 666 White, J.D.L., Ross, P.S., 2011. Maar-diatreme volcanoes: A review. J. Volc. Geotherm. Res. 201, 1–29.
667 doi:10.1016/j.jvolgeores.2011.01.010
- 668 Wilcock, W.S.D., Tolstoy, M., Waldhauser, F., Garcia, C., Tan, Y.J., Bohnenstiehl, D.R., Jacqueline Caplan-
669 Auerbach, R.P.D., Arnulf, A.F., Mann, M.E., 2016. Seismic constraints on caldera dynamics from the 2015
670 Axial Seamount eruption. Science 354, 1395–1399. doi:10.1107/S0021889808042726
- 671 Williams, H., 1941. Calderas and their origin. Univ. California Pub. Dept. Geol. Sci. 25, 239–346.
- 672 Wohletz, K.H., 2003. Water/Magma Interaction: Physical considerations for the deep submarine environment,
673 in: Explosive Subaqueous Volcanism, Geophysical Monograph Series. American Geophysical Union,
674 Washington, D. C., pp. 25–49. doi:10.1029/140GM02
- 675 Yokoyama, I., 1981. A geophysical interpretation of the 1883 Krakatau eruption. J. Volc. Geotherm. Res. 9,
676 359–378. doi:10.1016/0377-0273(81)90044-5
- 677 Zandomenighi, D., Barclay, A., Almendros, J., Ibañez Godoy, J.M., Wilcock, W.S.D., Ben-Zvi, T., 2009. Crustal
678 structure of Deception Island volcano from Pwave seismic tomography: Tectonic and volcanic implications.
679 J. Geophys. Res. 114, B06310. doi:10.1029/2008JB006119

680 Figure Captions

681

682 **Figure 1: PROTEUS seismic experiment.** Map of the sea bottom and land topography (Hooft et al., 2017)
683 and the layout of the entire marine-land dataset that was collected in November-December of 2015. The
684 dense seismic experiment recorded ~14,300 controlled-sound sources (beige dots) from the R/V Marcus
685 Langseth on 90 ocean-bottom and 65 land seismometers (yellow circles). The red rectangle shows the
686 region of this study and the islands and sedimentary basins are labelled. The black rectangle shows the
687 area that was averaged to obtain the velocity-depth curve for the reference metamorphic profile in Figure
688 5a.

689 **Figure 2. The geological and volcanic features of Santorini.** (a) Map of the sea bottom and land
690 topography (Hooft et al., 2017) showing the outcrops of pre-existing basement (yellow) including at the
691 summit of Profitis Ilias and the post-caldera volcanism (red) of the Kameni islands. (b) Gray-scale map of
692 topographic gradient showing the Mogi source at 4.5 km depth from GPS-InSAR inversion of 2011-2012
693 ground deformation (Parks et al., 2015) (red dot is best fit; colours RMS misfit). Volcanic features include
694 Kolumbo seamount (star), the Kolumbo and Kameni lineaments (dashed blue lines). The inset shows dike
695 strikes (Browning et al., 2015) for the Kolumbo lineament. (c) Vent locations for the four phases of the Late
696 Bronze Age explosive Plinian eruption. (d) Vents for the preceding 180 kyr of explosive Plinian eruptions
697 (white) and effusive caldera-filling shields (black).

698 **Figure 3. Maps of P-wave seismic velocity at Santorini.** Depth slices through the tomographic model at
699 400 m (a), 1 km (b), 1.6 km (c) and 2.8 km (d) depth below the seafloor. Contour interval is 0.2 km/s. In (a)
700 the grey lines show the profiles A-A' and B-B' in Figure 4 and the blue rectangle the area that was averaged
701 to obtain the velocity-depth curve for the caldera profile in Figure 5a. Note the cylindrical low velocity
702 anomaly in the upper 3 km beneath the north-central caldera with the most pronounced velocity reduction
703 between 1 and 2 km depth.

704 **Figure 4. Cross-sections of seismic velocity along profile A-A' and B-B'.** P-wave velocity and P-wave
705 velocity anomalies relative to the velocity-depth structure of the Anydros metamorphic block (Figure 5a)
706 along a NW-SE and a SE-NW profile. Contour interval is 0.2 km/s. Low velocities near the seafloor
707 delineate sedimentary basins on the flanks of the volcano. The deeper low-velocity anomaly at 1-2 km
708 depth north of the Kameni islands spatially correlates with the first three phases of the LBA eruption. The
709 topographic caldera corresponds with phase 4 of the LBA eruption. Higher velocities are inferred to be
710 due to metamorphic and/or plutonic rocks.

711 **Figure 5. Predicted porosity for the northern caldera low-velocity anomaly and the reference**
712 **metamorphic profile. (a)** The velocity-depth structure of the caldera (blue) and the reference metamorphic
713 profiles (black) obtained by averaging the velocity model over the blue and black rectangles in Figures 1
714 and 3. **(c)** The caldera velocity anomaly (dashed blue) is the difference between caldera and the reference
715 metamorphic profiles in **(a)**. **(b)** The porosity-depth structure is predicted for the reference profile (black)
716 using a pore aspect ratio of 0.05 corresponding to cracks. The range of caldera porosity structures (grey
717 field) corresponds to end-member pore aspect ratios from 0.5 (red) to 0.05 (blue) **(d)**. A geologically
718 motivated model where pore aspect ratio decreases with depth (grey) is also shown **(b & d)**. **(e)** A
719 correction to the predicted rock (dotted) and pore fluid (dot-dashed) velocities was applied for pressure
720 and temperature effects of hot caldera (blue) and cooler reference (black) geotherms. **(f)** For the
721 metamorphic profile we use 40°C/km for a volcanic back arc. The caldera geotherm is not well known and
722 gradients that varied by $\pm 40^\circ\text{C}/\text{km}$ (thin blue), and their corresponding effect on pore fluid and rock velocity
723 and on predicted porosity, are shown in **(e)** and **(b)**, respectively. See Text S1 for details.

724 **Figure 6. Conceptual model for the evolution of the LBA eruption and formation of the low-velocity**
725 **anomaly. (a)** Prior to the LBA eruption the Pre-Kameni island is located within a shallow caldera that
726 overlies the collapsed Skaros-Thirasia shields with their hyaloclastite cores. The Kameni and Kolumbo lines
727 (KL2 and KL1, respectively) exist and the magmatic system (red) is in a late stage of evolution. There may
728 be a low-density column (grey) between KL2 and KL1. **(b)** The inner cylindrical low-velocity anomaly is
729 spatially associated with phases 1, 2 and 3 of the LBA eruption that start Plinian and evolve to increasing
730 magma-water interactions with violent lithic ejection and tuff formation. **(c)** Collapse of the topographic
731 caldera and ignimbrite formation occurs during phase 4 of the LBA eruption. We infer the topographic
732 caldera forms by down-drop along inward-dipping normal faults potentially when accessing the deeper
733 part of the magmatic system. Three possible models to form the inner low-velocity anomaly during phases
734 1 to 3 of the eruption are: **(d)** Subsidence of pre-existing caldera fill and infill with ignimbrites and tuffs; **(e)**
735 Excavation by phreatomagmatic fracturing and reaming over a broad funnel-shaped venting region; **(f)**
736 Inner caldera collapse along outward-dipping reverse faults that fracture the pre-existing caldera fill.

737 **Figure 7. Comparison of the low-velocity anomaly with magma recharge during the 2011-2012 unrest**
738 **and predicted lithostatic pressure at 4 km depth. (a)** Conceptual model where unloading by the low-
739 density column favors intrusion, such as the 2011-2012 inflation, beneath the low-density column. A simple
740 lithostatic calculation suggests that spatial variations in unloading due to density variations in the upper
741 crust are of similar magnitude to those due to unloading by the topography of the volcano. **(b)** Lithostatic

742 *pressure calculated from the seismic velocity model. The variations in gravitational load due the*
743 *topography and the water column (c) are roughly equal to those from seismically-inferred crustal density*
744 *variations (d). Contour interval is 2 MPa.*

Figure 1

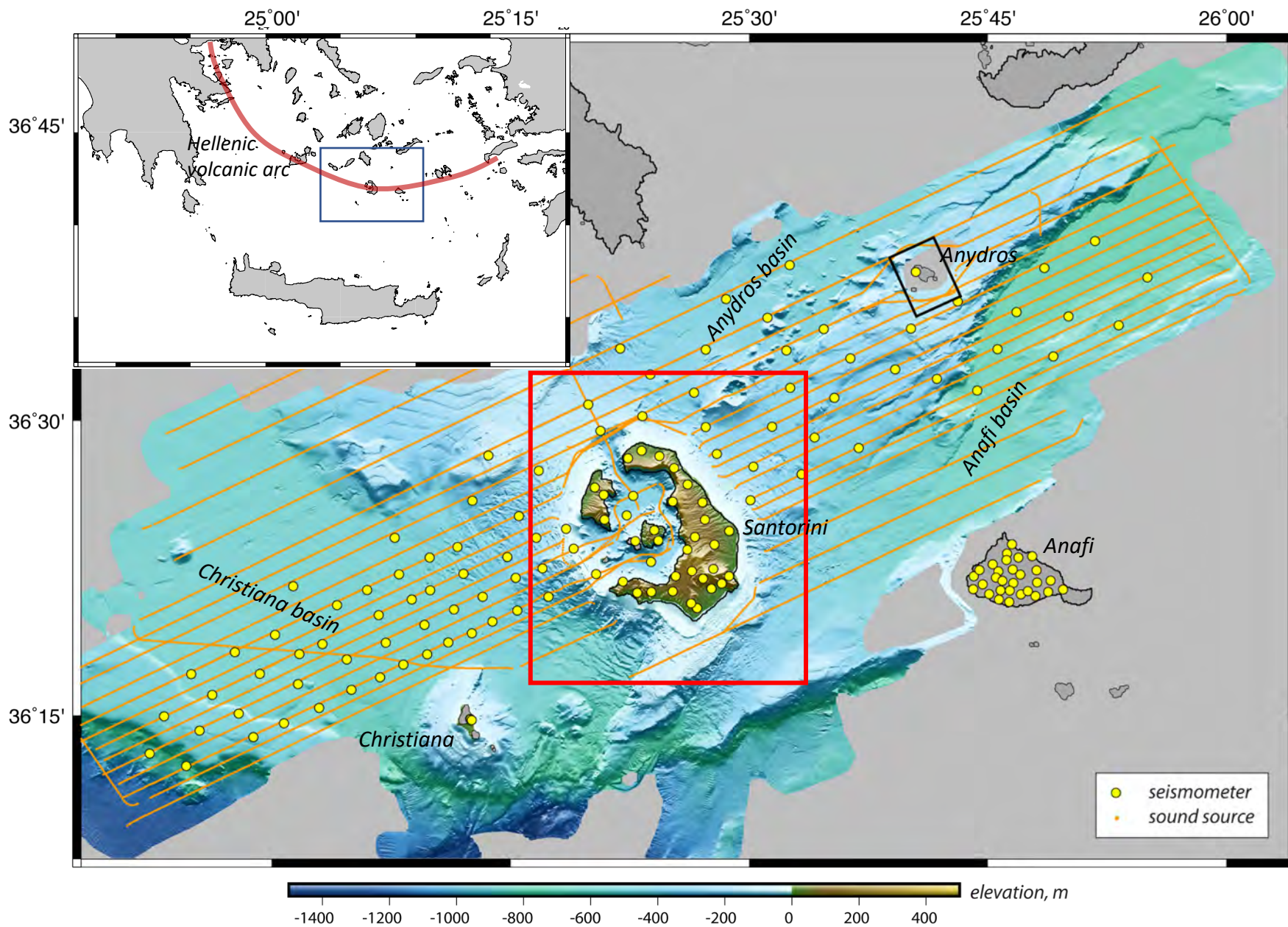


Figure 2

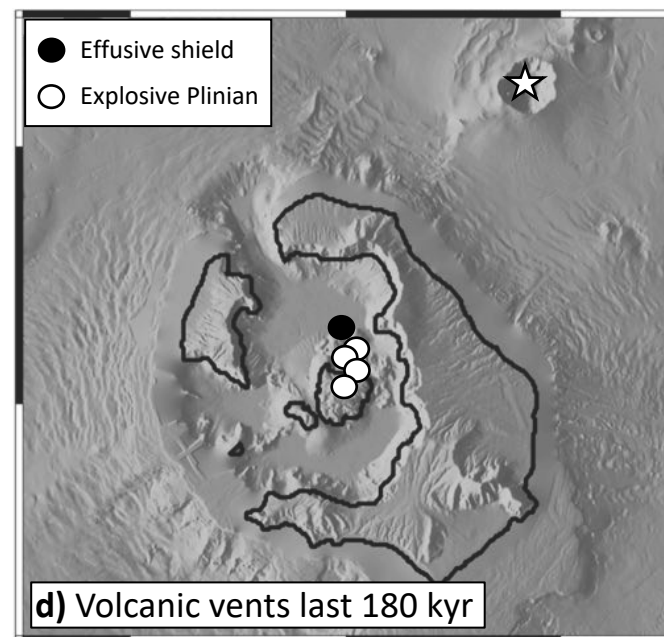
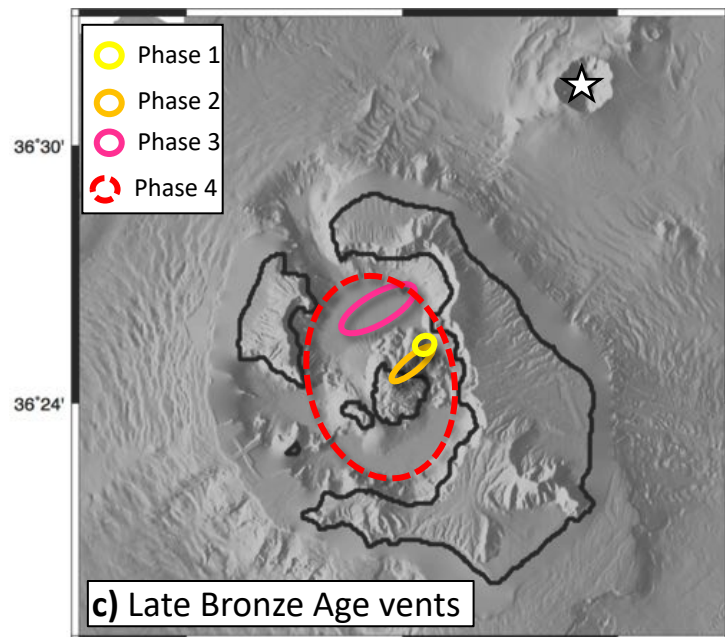
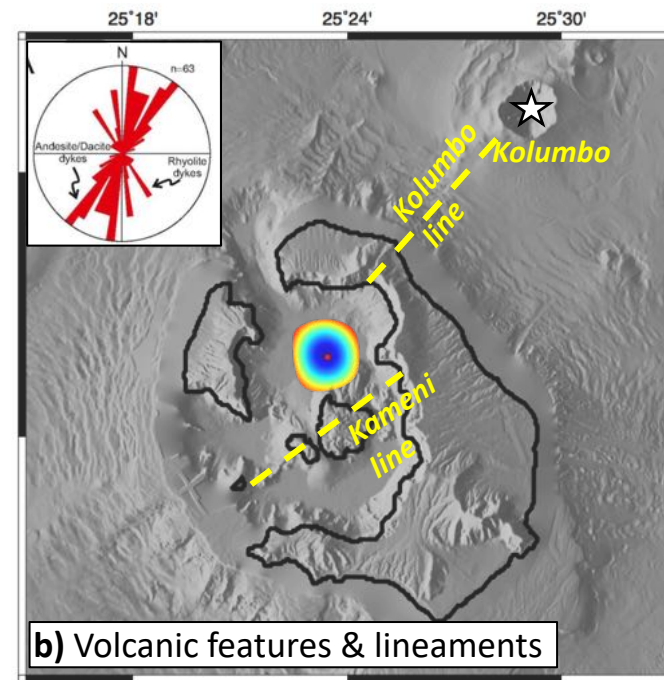
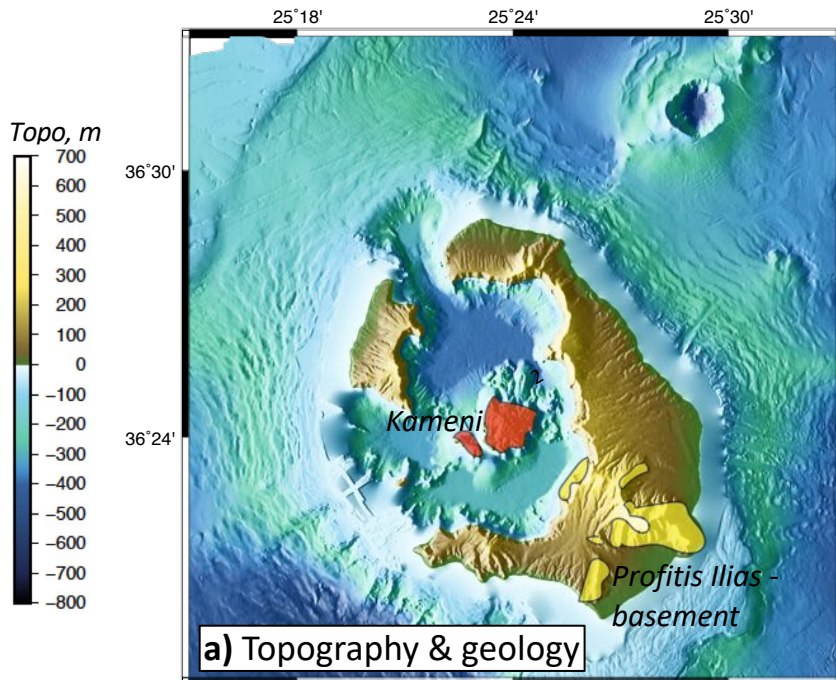


Figure 3

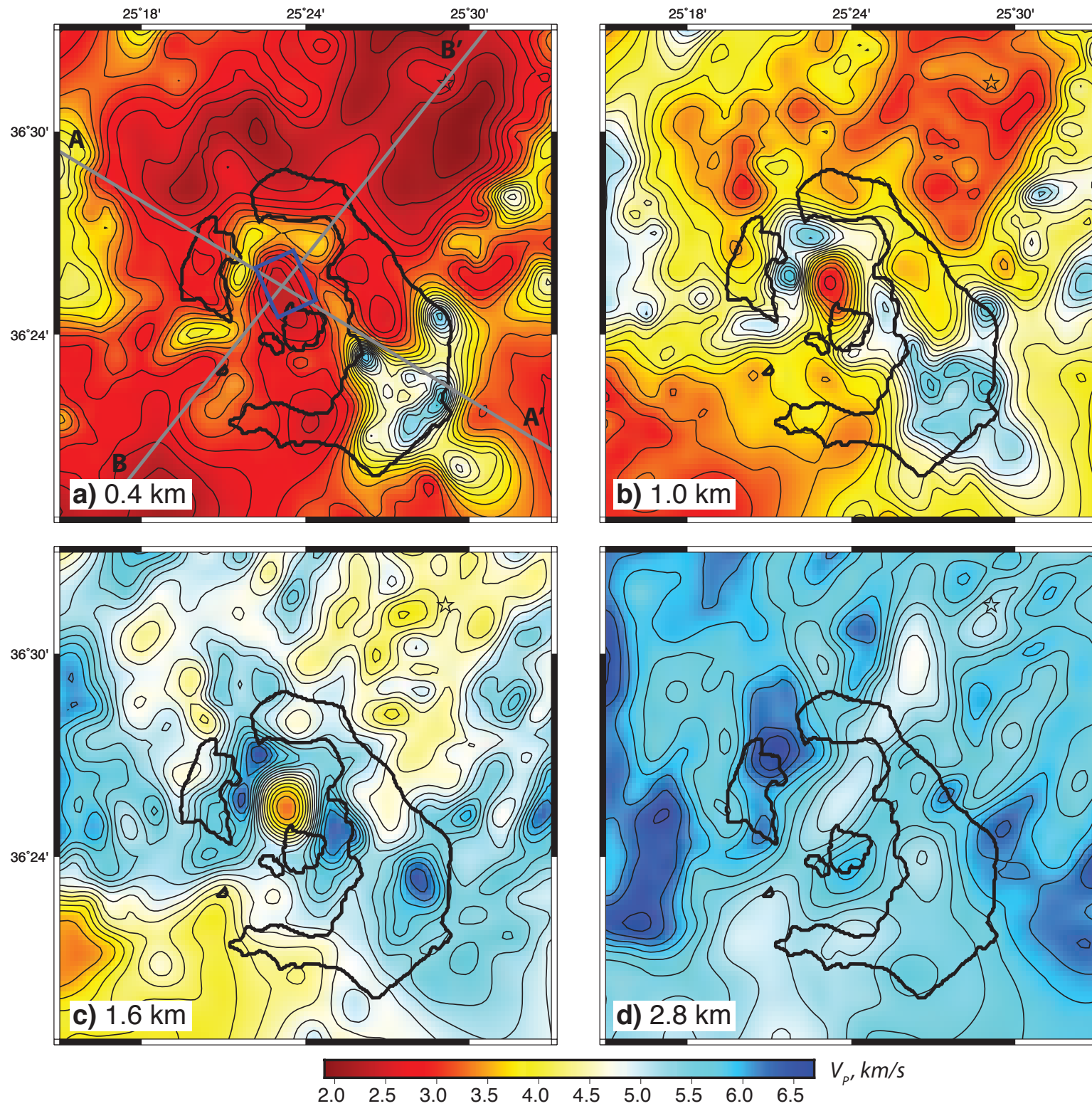


Figure 4

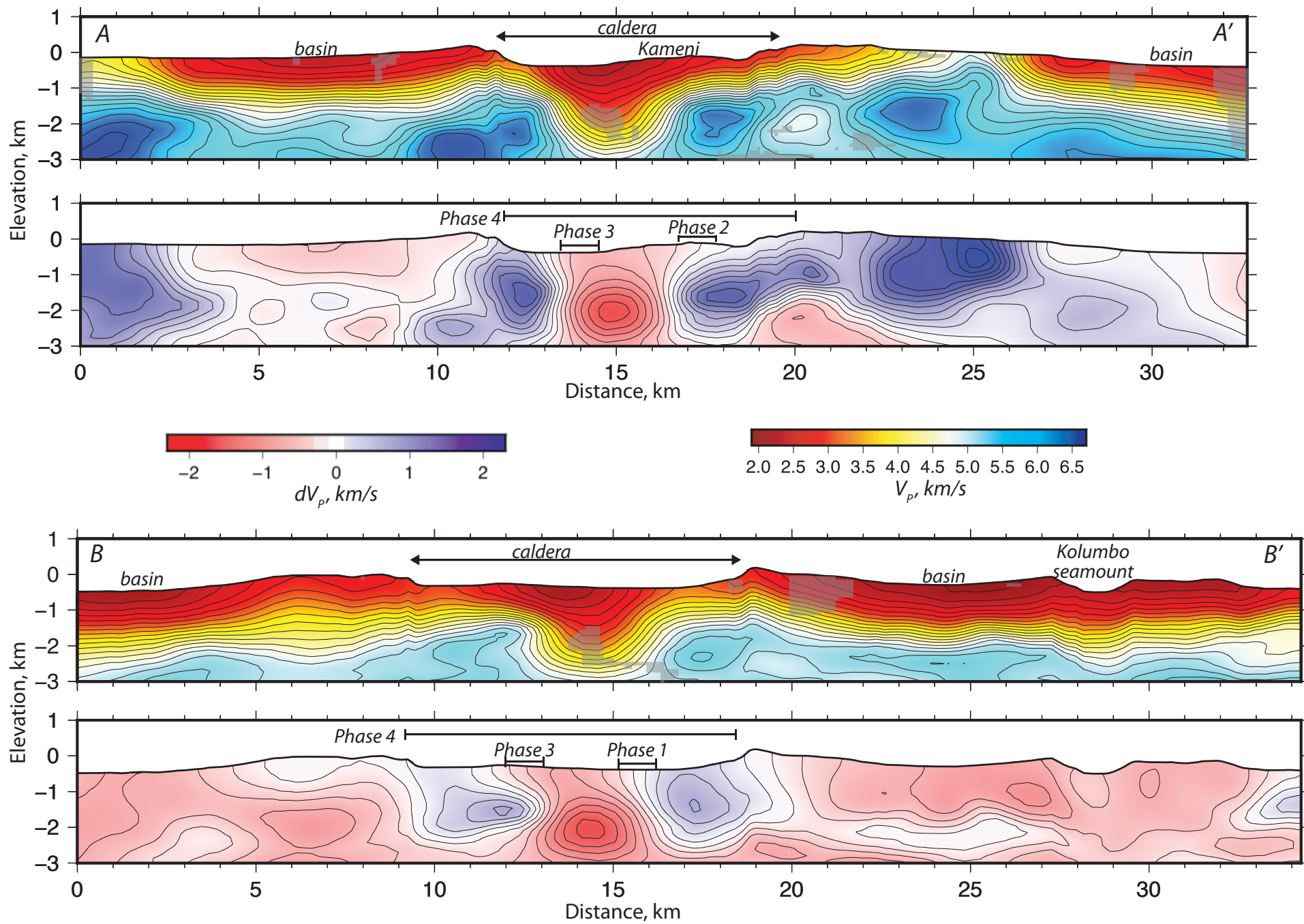


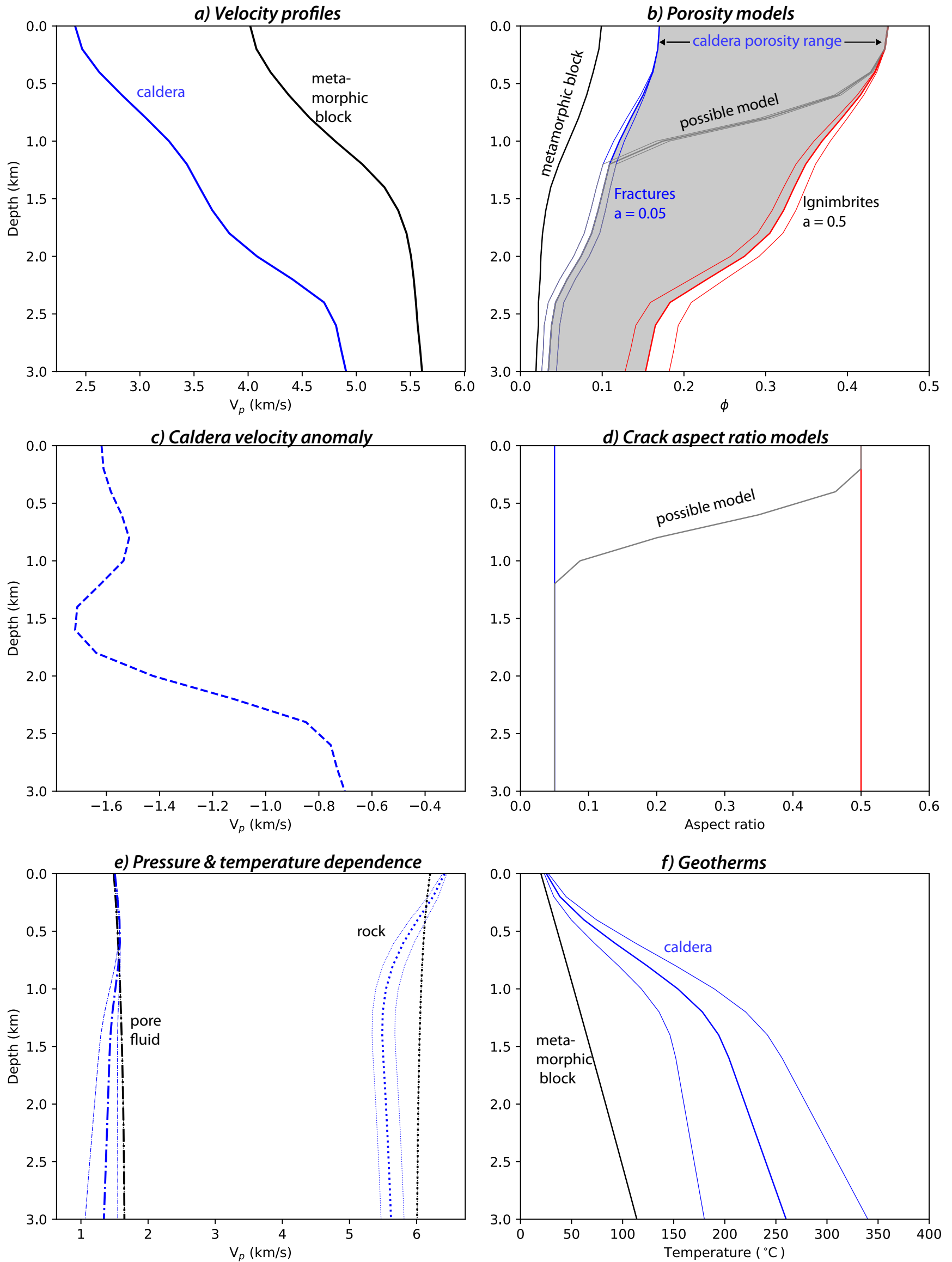
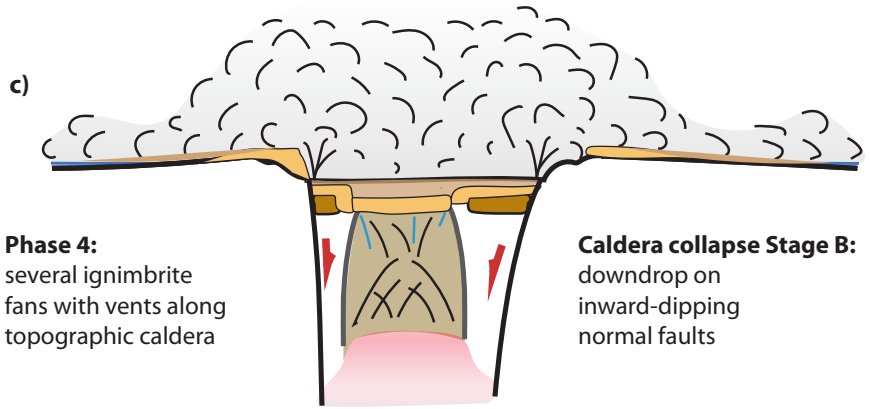
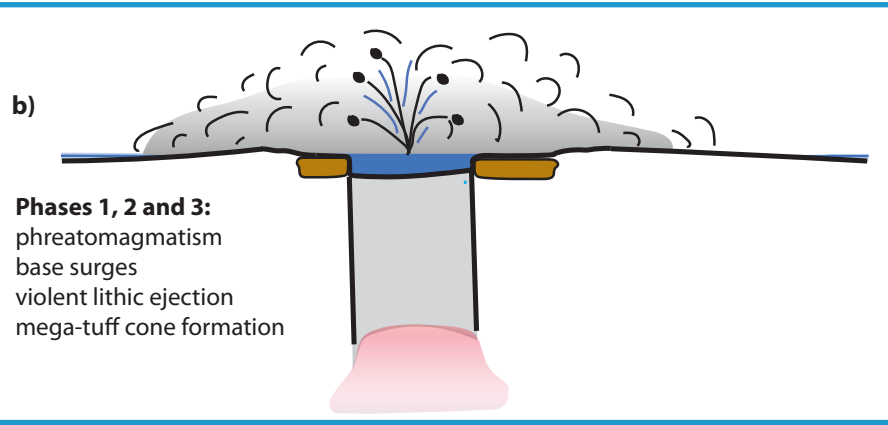
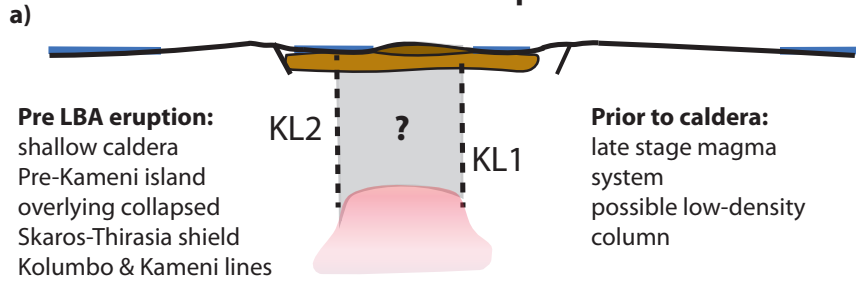
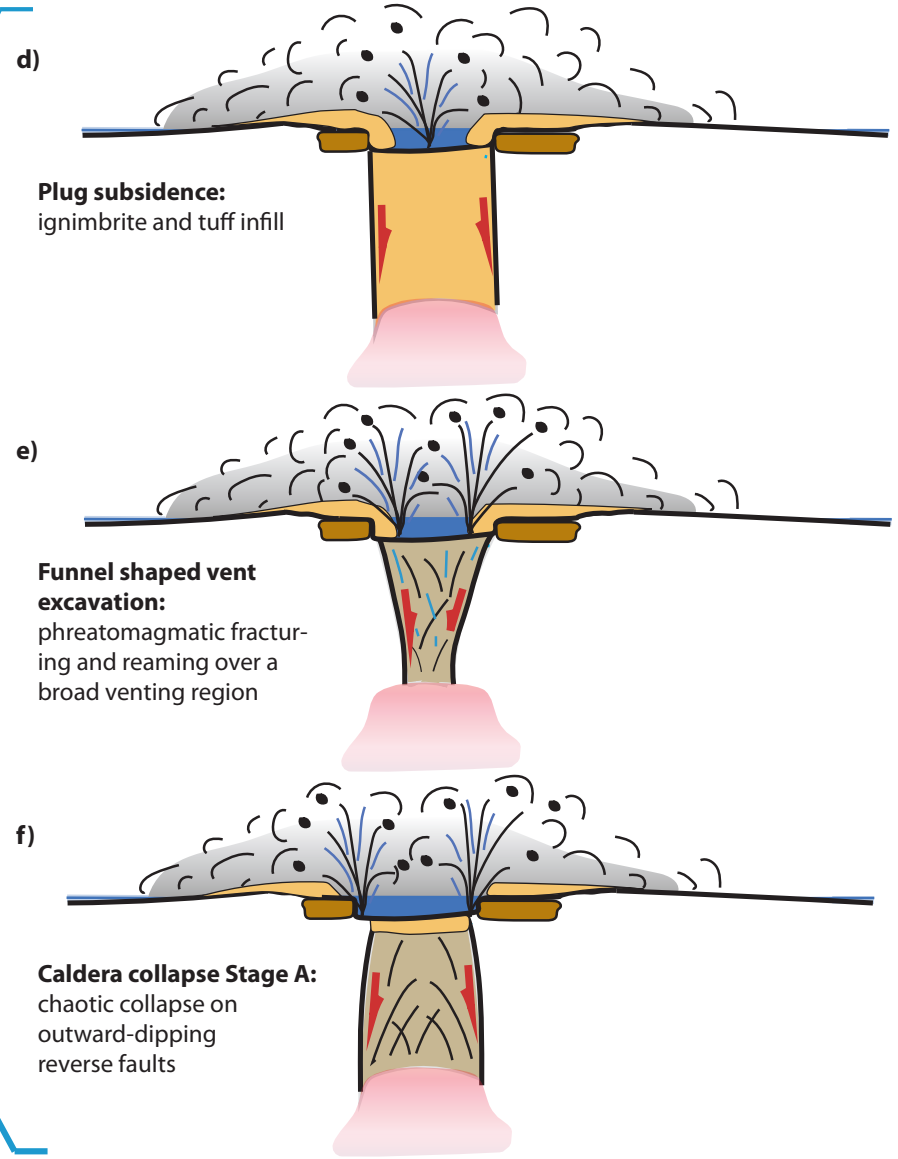
Figure 5

Figure 6

Evolution of LBA eruption



Low-velocity anomaly formation

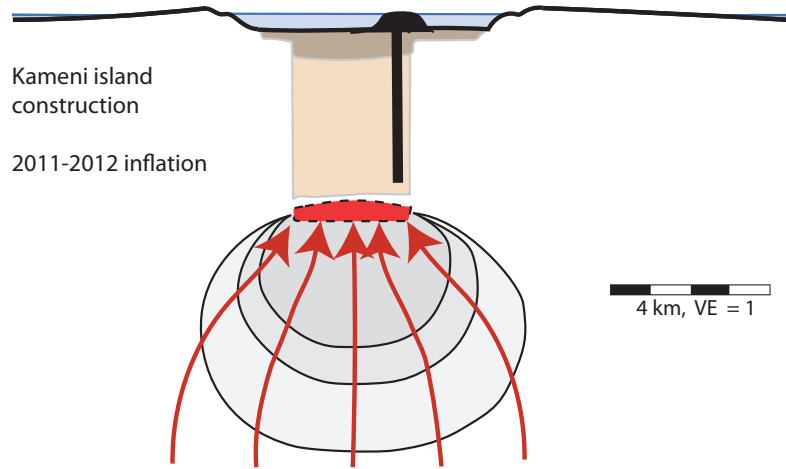


possible models

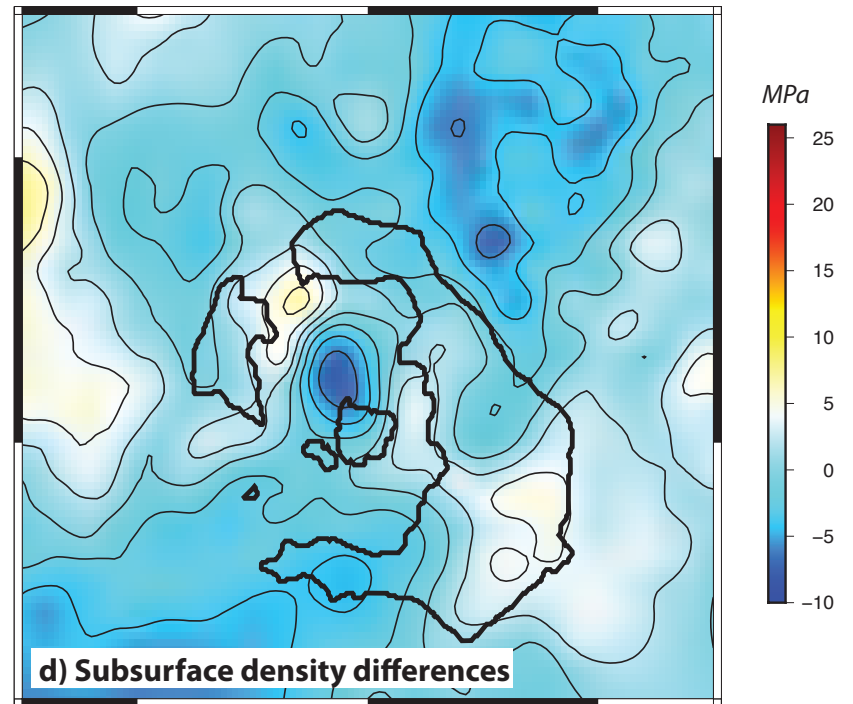
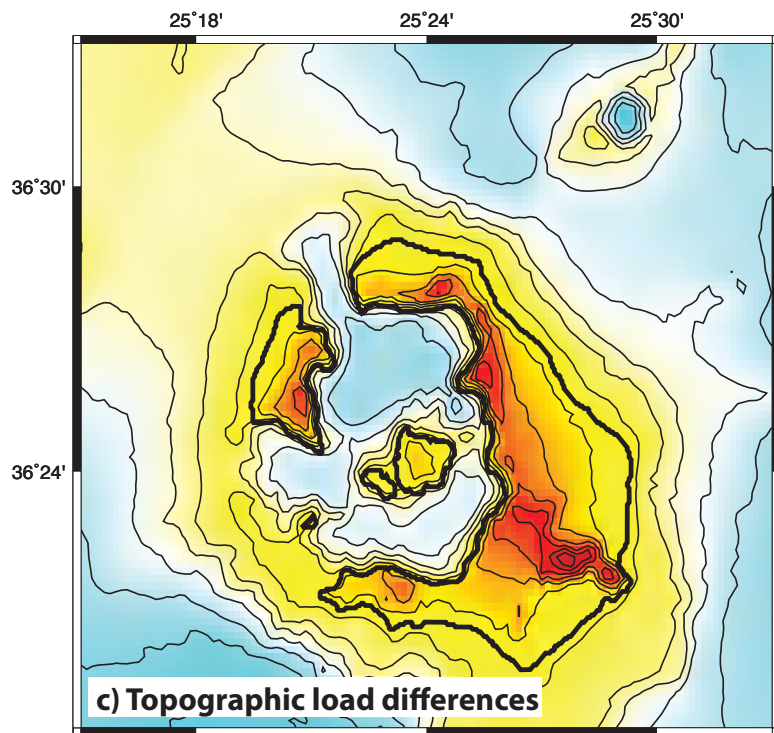
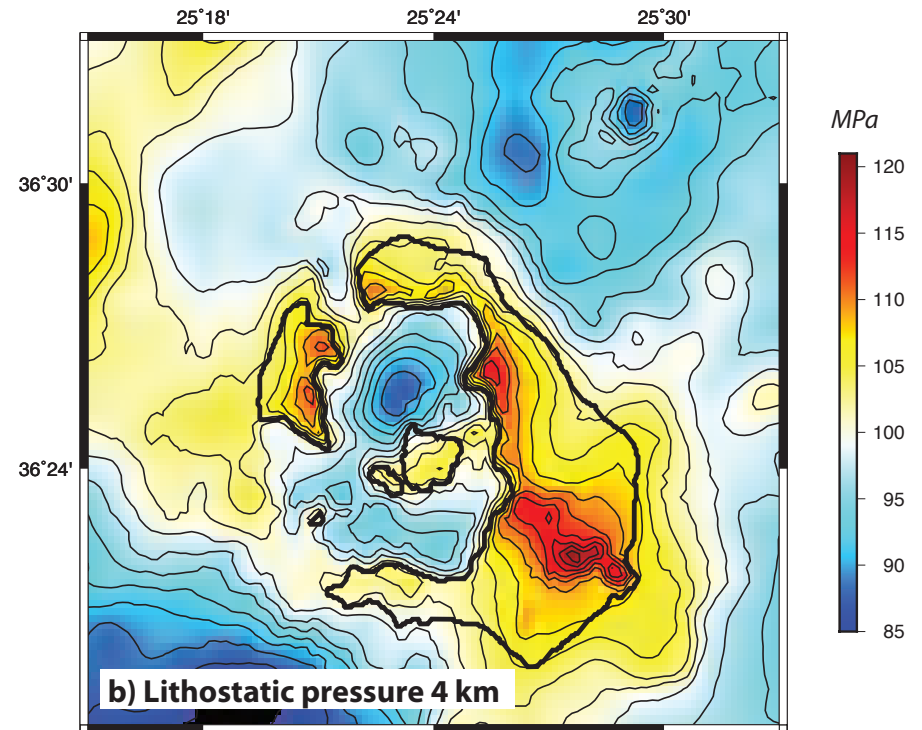
4 km, VE = 1

Figure 7

Post caldera volcanism: intrusions under high porosity column



a)



Supplementary material for online publication only

[Click here to download Supplementary material for online publication only: Supplementary Information V26-reduced.pdf](#)